



CrossMark  
click for updates

Cite this: *RSC Adv.*, 2016, 6, 21844

# Layer-by-layer assembled (high-energy carbon nanotube/conductive carbon nanotube)<sub>n</sub> nanocomposites for high volumetric capacitance supercapacitor electrodes†

Dongyeeb Shin, Yongmin Ko and Jinhan Cho\*

We introduce high-performance ultrathin electrochemical electrodes based on multi-stacking of high-energy multiwall carbon nanotube (MWCNT) hybrids and conductive MWCNTs. The MWCNT hybrids coated with oleic acid-stabilized pseudocapacitive nanoparticles (*i.e.*, OA-PC-MWCNTs) were assembled *via* a sequential covalent-bonded layer-by-layer (LbL) approach with amine-functionalized MWCNTs (NH<sub>2</sub>-MWCNT) in organic media, generating a highly porous structure and allowing for precise nanoscale control of the electrode thickness. The resultant NH<sub>2</sub>-MWCNT/OA-PC-MWCNT multilayer electrodes exhibited a high energy capacity and remarkable operational stability, considerably higher than the capacity and stability of conventional blended nanocomposite or electrostatic LbL-assembled electrodes. The volumetric capacitances of the (NH<sub>2</sub>-MWCNT/OA-Fe<sub>3</sub>O<sub>4</sub>-MWCNT)<sub>20</sub> and (NH<sub>2</sub>-MWCNT/OA-MnO-MWCNT)<sub>20</sub> were approximately 394 ± 10, and 674 ± 13 F cm<sup>-3</sup> at 1 A cm<sup>-3</sup>, respectively. Additionally, these electrodes maintained their high volumetric capacitances without loss of initial capacitance even after 10 000 cycles; this cycling stability stemmed from the formation of chemically stable covalent bonds between the MWCNT hybrids and NH<sub>2</sub>-MWCNTs and between the PC NPs and NH<sub>2</sub>-MWCNTs. Given that a variety of PC NPs can be used to prepare MWCNT hybrids and that this approach can be further expanded to nanocomposite films including LbL-assembled multilayers, our approach may provide a promising platform for designing electrodes for use as thin film-type energy storage devices.

Received 27th January 2016  
Accepted 18th February 2016

DOI: 10.1039/c6ra02461k

www.rsc.org/advances

## Introduction

The rapid growth in the use of sustainable and renewable energy sources such as the sun, wind and sea tide, as well as the development of various electronics, including electric vehicles and mobile electronics, has increased the need for efficient energy storage systems that can supply energy continuously.<sup>1–3</sup> Among the various energy storage systems, electrochemical capacitors based on an electrochemical double-layer mechanism have high power density and low energy density, which makes them suitable for high-power applications such as load leveling devices for heavy machinery or integrated power supplies for microscale devices.<sup>4,5</sup> Batteries have high energy density because of the full usage of their electrodes, but

additional time is required for the stored charge to enter and leave the electrodes, resulting in a lower power density and a substantial volume change of the electrodes during charge and discharge.<sup>6–8</sup> Although supercapacitors, which can fill the gap between conventional electrochemical capacitors and lithium-ion batteries, have attracted considerable attention as an excellent candidate for energy storage systems, their performance should be improved further for electronics requiring power sources with higher energy storage and longer lifetimes.<sup>9–13</sup>

Recent research efforts have focused on the development of promising supercapacitor electrode materials composed of pseudocapacitive nanoparticles (PC NPs) with high specific capacitance and electrically conductive materials with large surface areas such as multiwall carbon nanotubes (MWCNTs), reduced graphene oxides or mesoporous carbon.<sup>14–17</sup> Although ruthenium oxide (RuO<sub>2</sub>) NPs exhibit a theoretically high specific mass capacitance (>1000 F g<sup>-1</sup>) among the various electrode materials, the high cost of RuO<sub>2</sub> has limited its commercial viability for supercapacitor applications. In this regard, magnetite (Fe<sub>3</sub>O<sub>4</sub>) and manganese oxide (MnO<sub>2</sub> or MnO), which have different valence states, have emerged as promising

Department of Chemical and Biological Engineering, Korea University, Anam-dong, Seongbuk-gu, Seoul 136-713, Korea. E-mail: jinhan71@korea.ac.kr

† Electronic supplementary information (ESI) available: Experimental details for the material preparation, contact angles of the NH<sub>2</sub>-MWCNT/OA-Fe<sub>3</sub>O<sub>4</sub>-MWCNT multilayers, TGA date of OA-Fe<sub>3</sub>O<sub>4</sub>-MWCNT hybrids, magnetic curve of OA-Fe<sub>3</sub>O<sub>4</sub>-MWCNT hybrids, HR-TEM images of aqueous anionic octakis-Fe<sub>3</sub>O<sub>4</sub>-MWCNTs, electrochemical performances of NH<sub>2</sub>-MWCNT/OA-Fe<sub>3</sub>O<sub>4</sub>-MWCNT multilayer. See DOI: 10.1039/c6ra02461k

electrode materials because of their low cost and environmentally benign nature.<sup>18–23</sup> However, in most cases, these PC materials have been simply solution-blended or electrostatically bonded with conductive materials without serious consideration of the amount of PC NPs adsorbed onto conductive materials and/or the interfacial stability between PC NPs and conductive materials, which has limited the improvement of the energy storage capacity and the cycling stability. More recently, the high demand for a variety of microscale or miniaturized energy storage devices with high efficiency has prompted the development of ultrathin supercapacitor electrodes with high volumetric capacitance in a limited electrode volume instead of specific mass capacitance.<sup>24–26</sup>

Recently, electrostatic layer-by-layer (LbL) assembly methods allowing for the nanoscale blending of several functional electrode materials in aqueous media have demonstrated that various charged NPs can be easily incorporated into oppositely charged conductive matrices by electrostatic interaction in aqueous media. This approach can produce binder-free ultrathin films with highly controllable thickness up to the micrometer scale, irrespective of electrode size and shape.<sup>27–29</sup> However, this electrostatic LbL assembly method has difficulty in significantly increasing the total film thickness as well as the amount of NPs adsorbed because of long-range electrostatic repulsion occurring among NPs with the same charge.<sup>30</sup> Additionally, the relatively weak electrostatic bonding between NPs and conductive materials causes desorption of the NPs onto the conductive materials during repetitive charge/discharge operations, as previously mentioned. As a result, despite the various advantages of electrostatic LbL assembly, these phenomena act as drawbacks that restrict the high volumetric capacitance and long-term stability of thin film-type energy storage devices. To our knowledge, the various electrostatic LbL-assembled electrodes such as (MWCNT/MnO<sub>2</sub>)<sub>n</sub> and (MWCNT/TiO<sub>2</sub>)<sub>n</sub> electrodes display a volumetric capacitance of approximately 200–250 F cm<sup>-3</sup> (at 1 mV s<sup>-1</sup>) with approximately 8–10% loss of initial capacitance after 1000 cycles.

Herein, we report ultrathin film-type supercapacitor electrodes *via* the covalently bonded LbL assembly of high-energy MWCNT hybrids and conductive MWCNTs; the resulting electrodes display excellent volumetric capacitance and long-term cycling stability. First, for the preparation of these high-energy MWCNT hybrids, the well-defined OA-PC NPs (*i.e.*, OA-Fe<sub>3</sub>O<sub>4</sub> or OA-MnO NPs) synthesized in toluene were densely deposited onto amine-functionalized MWCNTs (*i.e.*, NH<sub>2</sub>-MWCNTs) *via* a ligand exchange reaction<sup>31</sup> between the OA ligands of the NPs and the NH<sub>2</sub> groups of the MWCNTs. The mass density of these MWCNT hybrids were 1.65 ± 0.02 g cm<sup>-3</sup>.

The formed OA-PC-MWCNT hybrids were highly dispersible in nonpolar media without the aid of an additional surfactant. As previously noted,<sup>31,32</sup> the OA-PC-coated MWCNT hybrids were further LbL-assembled with NH<sub>2</sub>-MWCNTs *via* the same ligand-exchange reaction for the preparation of ultrathin film electrodes with a highly uniform and chemically stable structure, allowing for precise thickness control. That is, these MWCNT hybrids can be used as a high-energy storage component with a large surface area and simultaneously as a building

block for the LbL-assembled electrodes. Additionally, our ligand-exchange LbL assembly approach for the formation of OA-PC-MWCNT hybrids/MWCNT film in organic media does not require complex assembly conditions (for instance, the pH value and ionic strength of the deposition solution that should be considered in traditional electrostatic LbL assembly), and furthermore allows for more facile and scalable thickness control than traditional LbL assembly methods (based on the repetitive deposition of PC NPs and MWCNTs) including electrostatic LbL assembly. To our knowledge, the LbL assembly of films (or electrodes) using high-energy MWCNT hybrids (*i.e.*, MWCNT hybrids densely coated with pseudocapacitive or metal oxide NPs) has not been previously reported.

The volumetric capacitances of the (NH<sub>2</sub>-MWCNT/OA-Fe<sub>3</sub>O<sub>4</sub>-MWCNT)<sub>20</sub> electrodes were approximately 394 ± 10 F cm<sup>-3</sup> at 1 A cm<sup>-3</sup> in neutral electrolyte solution instead of a harsh acidic solution. This volumetric capacitance was significantly (more than three-fold) higher than the volumetric capacitance of conventional supercapacitor electrodes based on carbon-based materials and iron oxide NPs. The volumetric capacitances of the (NH<sub>2</sub>-MWCNT/OA-MnO-MWCNT)<sub>20</sub> samples were further increased up to 674 ± 13 F cm<sup>-3</sup> at 1 A cm<sup>-3</sup>, which is also superior to the volumetric capacitances of other manganese oxide-based supercapacitor electrode.<sup>29</sup> Additionally, these electrodes maintained high electrochemical performance without loss of their initial capacitance, even after 10 000 cycles. Furthermore, given that many researchers have attempted to combine MWCNTs with metal oxide NPs, including PC NPs, to prepare materials for various other applications, including microwave absorbers, gas sensors, and catalysts, in addition to materials for energy storage devices, we believe that our approach of using ligand-exchange-induced MWCNT hybrids may provide a basis for exploiting and designing hybrid nanocomposites with tailored functionalities and high performance.

## Experimental

Experimental details are shown in ESI.†

## Results and discussion

Our strategy for ultrathin multilayered electrode composed of PC NP-coated MWCNTs and MWCNTs is shown in Fig. 1. First, the NH<sub>2</sub>-MWCNTs<sup>33–35</sup> dispersed in ethanol and the well-defined OA-Fe<sub>3</sub>O<sub>4</sub> NPs<sup>31,36</sup> with a diameter of approximately 8 ± 1 nm in toluene were prepared as described in Experimental.† For the preparation of OA-Fe<sub>3</sub>O<sub>4</sub> NP-coated NH<sub>2</sub>-MWCNT (*i.e.*, OA-Fe<sub>3</sub>O<sub>4</sub>-MWCNT) hybrids, 10 mg mL<sup>-1</sup> OA-Fe<sub>3</sub>O<sub>4</sub> NP toluene solution was mixed with NH<sub>2</sub>-MWCNT ethanol solution with a concentration of 1 mg mL<sup>-1</sup>. In this case, the NH<sub>2</sub>-MWCNTs were phase-transferred from an alcohol to a toluene solution because of the high affinity between the surface of the Fe<sub>3</sub>O<sub>4</sub> NP and the NH<sub>2</sub> groups of the NH<sub>2</sub>-MWCNT. These OA-Fe<sub>3</sub>O<sub>4</sub>-MWCNT hybrids with high dispersion stability in toluene also have a high affinity for NH<sub>2</sub>-MWCNTs.

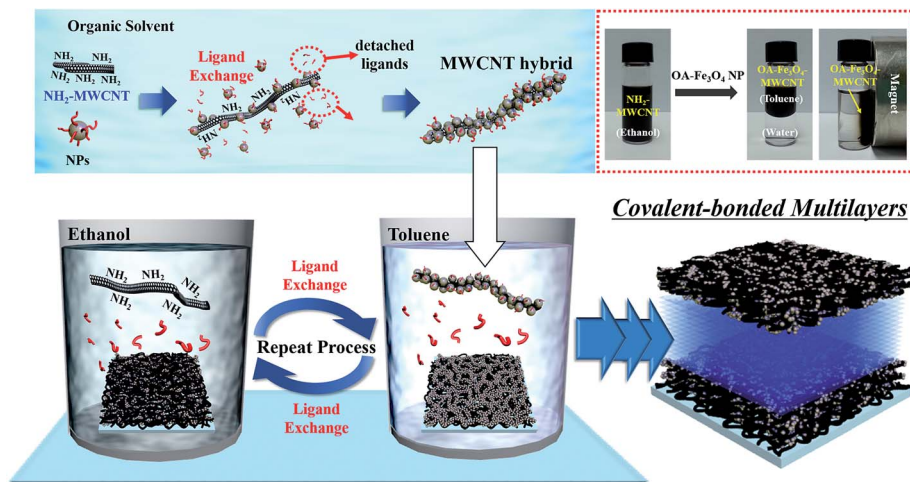


Fig. 1 Schematic diagram showing the preparation of OA-PC-MWCNT hybrids and  $(\text{NH}_2\text{-MWCNT/OA-PC-MWCNT})_n$  multilayer film using ligand exchange reaction. In the case of OA- $\text{Fe}_3\text{O}_4$ -MWCNTs with high dispersion stability in toluene, they displayed the strong magnetic properties due to the densely coated  $\text{Fe}_3\text{O}_4$  NPs onto MWCNTs.

This high affinity was confirmed by FTIR in transmission and attenuated total reflectance (ATR) modes. First, the C-H stretching ( $2854$  and  $2925\text{ cm}^{-1}$ ) and  $\text{COO}^-$  stretching ( $1411$  and  $1540\text{ cm}^{-1}$ ) modes originated from carboxylate ion groups and the long aliphatic chains of the OA ligands loosely bound to  $\text{Fe}_3\text{O}_4$  NPs, respectively. Additionally, the N-H bending ( $1640\text{ cm}^{-1}$ ) and N- $\text{CH}_3$  stretching ( $1372\text{ cm}^{-1}$ ) modes corresponded to the amine groups of  $\text{NH}_2$ -MWCNTs.<sup>35,37–39</sup> Therefore, OA- $\text{Fe}_3\text{O}_4$ -MWCNT hybrids exhibited the characteristic absorption peaks ( $1372$ ,  $1411$ ,  $1540$ , and  $1640\text{ cm}^{-1}$ ) assigned to the OA ligands and  $\text{NH}_2$  groups (Fig. 2a). To better understand this adsorption mechanism, we investigated the traces of the C-H stretching peaks of OA ligands through the additional adsorption of the  $\text{NH}_2$ -MWCNTs onto the outermost OA- $\text{Fe}_3\text{O}_4$  NP layer-coated substrate (*i.e.*,  $(\text{NH}_2\text{-MWCNT/OA-Fe}_3\text{O}_4\text{-MWCNT/NH}_2\text{-MWCNT})$ -coated Si substrate) (Fig. 2b). In this case, the peak intensity of the C-H stretching modes gradually decreased, and the intensity of the N-H bending and N- $\text{CH}_3$  stretching peaks intensified as the adsorption time for the  $\text{NH}_2$ -MWCNTs was increased from 0 min to 1 day. These phenomena imply that the OA ligands loosely bound to the surface of  $\text{Fe}_3\text{O}_4$  NPs were replaced by the  $\text{NH}_2$  groups of  $\text{NH}_2$ -MWCNTs. Furthermore, they imply that the interfaces of the  $\text{Fe}_3\text{O}_4$  NPs and MWCNTs were bridged to the  $-\text{NH}_2$  groups. However, the outermost surfaces of the hybrids were still stabilized by hydrophobic OA ligands bound to the surface of  $\text{Fe}_3\text{O}_4$  NPs. These phenomena were also confirmed by the fact that water contact angles for the outermost  $\text{NH}_2$ -MWCNT and OA- $\text{Fe}_3\text{O}_4$ -MWCNT hybrids were approximately  $88 \pm 4^\circ$  and  $132 \pm 6^\circ$ , respectively (Fig. S1†).

On the basis of the aforementioned results, we investigated the surface morphology of the OA- $\text{Fe}_3\text{O}_4$ -MWCNT hybrids using high-resolution transmission electron microscopy (HR-TEM). As shown in Fig. 2c, the well-defined OA- $\text{Fe}_3\text{O}_4$  NPs were densely and uniformly adsorbed onto the  $\text{NH}_2$ -MWCNTs, constituting a loading amount of approximately 57.3 wt%

(Fig. S2†). These hybrids also displayed superparamagnetic properties with a relatively high saturated magnetism of  $50\text{ emu g}^{-1}$  at room temperature (Fig. S3†). Although various approaches, including electrostatic interactions and the ion-reduction method, have been used to prepare metal oxide NP-coated MWCNT (or single-walled CNT) hybrids,<sup>40–43</sup> the degree of adsorption of metal oxide NPs onto the MWCNTs has typically been limited to a decoration level with a low packing density ( $<30\%$ ) in the lateral dimension (Fig. S4†). Cao *et al.* have reported that  $\text{Fe}_3\text{O}_4$ -MWCNT hybrids prepared by the ion reduction process in aqueous solution exhibit a saturation magnetization of  $30\text{ emu g}^{-1}$ .<sup>44</sup> Additionally, other metal oxide nanoparticles (*i.e.*, OA- $\text{TiO}_2$  and OA- $\text{BaTiO}_3$  NPs) as well as OA- $\text{Fe}_3\text{O}_4$  NPs could also be densely deposited onto the  $\text{NH}_2$ -MWCNTs *via* a ligand exchange mechanism (Fig. S5†).

An additional benefit of our approach is that the OA- $\text{Fe}_3\text{O}_4$ -MWCNT hybrids could be consecutively LbL-assembled with the  $\text{NH}_2$ -MWCNTs, generating a high loading amount (or layer thickness) per layer and a porous structure (by the formation of voids between OA-PC-MWCNTs and  $\text{NH}_2$ -MWCNTs), which is effective for the preparation of LbL-assembled supercapacitor electrodes requiring high energy density, facile charge transfer and large surface area (see Fig. 1). To demonstrate this possibility, the adsorbed amount and film thickness of LbL-assembled  $\text{NH}_2$ -MWCNT/OA- $\text{Fe}_3\text{O}_4$ -MWCNT multilayer films were quantitatively investigated using a quartz crystal microbalance (QCM)<sup>45</sup> and cross-sectional SEM images. The frequency changes,  $\Delta F$  (or mass changes,  $\Delta m$ ), per layer measured from alternating depositions of OA- $\text{Fe}_3\text{O}_4$ -MWCNT hybrids (concentration of approximately  $11\text{ mg mL}^{-1}$ ) in toluene and  $\text{NH}_2$ -MWCNTs ( $1\text{ mg mL}^{-1}$ ) in ethanol were  $111.8 \pm 10\text{ Hz}$  ( $\Delta m \approx 1975\text{ ng cm}^{-2}$ ) and  $16.4 \pm 5\text{ Hz}$  ( $\Delta m \approx 289\text{ ng cm}^{-2}$ ), respectively (Fig. 3a). The total thickness and mass density of the 20-bilayered film with a porous structure was approximately  $241\text{ nm}$  (*i.e.*, a thickness per bilayer of approximately  $12\text{ nm}$ ) (Fig. 3b) and  $1.65 \pm 0.02\text{ g cm}^{-3}$ , respectively

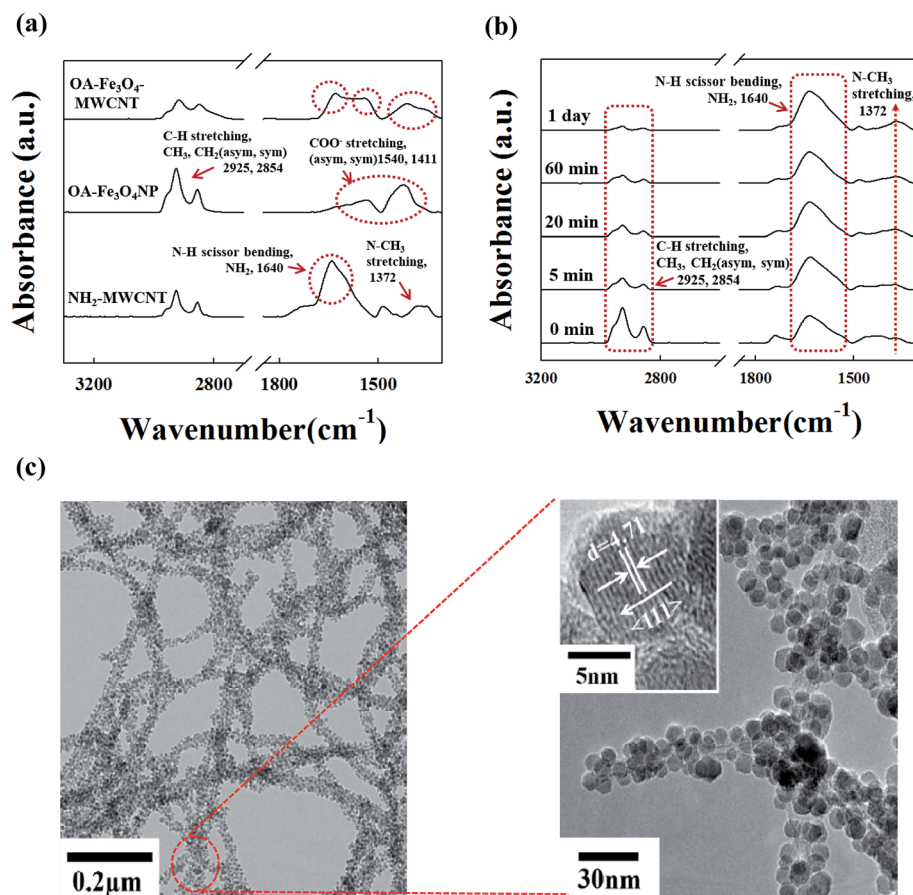


Fig. 2 (a) FTIR spectra of NH<sub>2</sub>-MWCNTs, OA-Fe<sub>3</sub>O<sub>4</sub> NPs, and OA-Fe<sub>3</sub>O<sub>4</sub>-MWCNTs. (b) FT-IR spectra of the (NH<sub>2</sub>-MWCNT/OA-Fe<sub>3</sub>O<sub>4</sub>-MWCNT)-coated Si substrate as a function of adsorption time of NH<sub>2</sub>-MWCNT. (c) HR-TEM images of the OA-Fe<sub>3</sub>O<sub>4</sub>-MWCNT hybrids.

(Experimental† and Fig. 3c). However, in the case of electrostatically LbL-assembled NH<sub>3</sub><sup>+</sup>-MWCNT/anionic octakis-Fe<sub>3</sub>O<sub>4</sub>-MWCNT multilayer films, their mass changes per layer and film thicknesses were notably lower than those of the NH<sub>2</sub>-MWCNT/OA-Fe<sub>3</sub>O<sub>4</sub>-MWCNT multilayer films and resulted in a mass density of  $1.14 \pm 0.03 \text{ g cm}^{-3}$  (Fig. 3d). This electrostatic LbL assembly places an upper limit on the loading amount of charged components because of the long-range electrostatic repulsion between components with the same charges during deposition. Additionally, the high loading amount shown in the NH<sub>2</sub>-MWCNT/OA-Fe<sub>3</sub>O<sub>4</sub>-MWCNT multilayers could be further increased by controlling the solution concentration of the OA-Fe<sub>3</sub>O<sub>4</sub>-MWCNT hybrids. As shown in Fig. 3e, the bilayer thickness of the NH<sub>2</sub>-MWCNT/OA-Fe<sub>3</sub>O<sub>4</sub>-MWCNT multilayer films was increased from 12 to 35 nm when the solution concentration of the OA-Fe<sub>3</sub>O<sub>4</sub>-MWCNT hybrids was increased from 11 to 22 mg mL<sup>-1</sup>. Additionally, the 1.37 μm-thick (NH<sub>2</sub>-MWCNT/22 mg mL<sup>-1</sup> OA-Fe<sub>3</sub>O<sub>4</sub>-MWCNT)<sub>40</sub> film exhibited a highly porous but uniform structure, with no agglomeration. These results show that our approach has excellent processing efficiency, allowing for a high loading amount, and creates a uniform surface/internal structure.

The electrical properties of the NH<sub>2</sub>-MWCNT/OA-Fe<sub>3</sub>O<sub>4</sub>-MWCNT multilayers were examined by measuring their sheet

resistance and electrical conductivity using the four-point probe method. As shown in Fig. 4a, the sheet resistance and electrical conductivity of the multilayer films prepared from the hybrid solution of 11 mg mL<sup>-1</sup> decreased from  $7.1 \times 10^8$  to  $9.0 \times 10^7 \text{ } \Omega \text{ sq}^{-1}$  and increased from 0.01 to 0.04 S m<sup>-1</sup> as the bilayer number ( $n$ ) increased from 5 (thickness of approximately 70 nm) to 20 (thickness of approximately 241 nm). Although the sheet resistance of the hybrid-based multilayers was higher than the  $6.8 \times 10^6 \text{ } \Omega \text{ sq}^{-1}$  value for the (NH<sub>3</sub><sup>+</sup>-MWCNT/anionic octakis-Fe<sub>3</sub>O<sub>4</sub>-MWCNT)<sub>20</sub> films, the increased percolation of the NH<sub>2</sub>-MWCNTs enhanced the electrical conductivity of the hybrid-based films by increasing the number of bilayers despite the dense packing of the OA-Fe<sub>3</sub>O<sub>4</sub> NPs with high resistivity ( $>10^{12} \text{ } \Omega \text{ sq}^{-1}$ ) onto the MWCNTs. In the case of the multilayer film composed of OA-Fe<sub>3</sub>O<sub>4</sub> NPs and insulating poly(ethylene imine) (PEI), the sheet resistance was not measured because its high resistivity exceeded the gauge range. These phenomena were also confirmed by EIS measurements of the 241 nm-thick NH<sub>2</sub>-MWCNT/OA-Fe<sub>3</sub>O<sub>4</sub>-MWCNT and 237 nm-thick PEI/OA-Fe<sub>3</sub>O<sub>4</sub>-MWCNT multilayer electrodes (Fig. S6†). In this case, the equivalent series resistance values of the NH<sub>2</sub>-MWCNT/OA-Fe<sub>3</sub>O<sub>4</sub>-MWCNT and PEI/OA-Fe<sub>3</sub>O<sub>4</sub>-MWCNT multilayer films were 39 and 45 Ω, respectively. These results suggest that the NH<sub>2</sub>-MWCNTs can operate as continuous conductive pathways

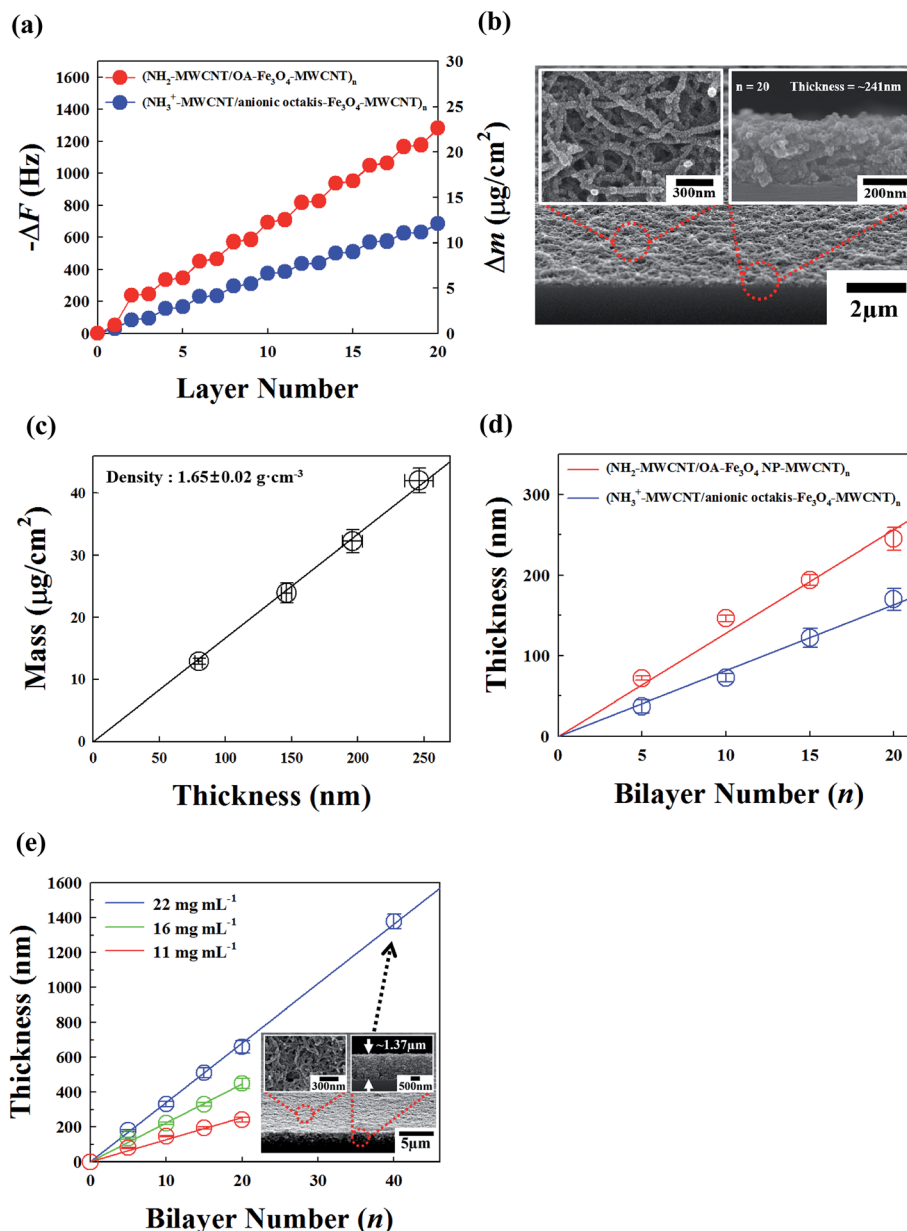


Fig. 3 (a) Frequency ( $\Delta F$ ) and mass change ( $\Delta m$ ) of the  $(\text{NH}_2\text{-MWCNT/OA-Fe}_3\text{O}_4\text{-MWCNT})_n$  and  $(\text{NH}_3^+\text{-MWCNT/anionic octakis-Fe}_3\text{O}_4\text{-MWCNT})_n$  films as a function of the layer number. (b) FE-SEM images of the  $(\text{NH}_2\text{-MWCNT/OA-Fe}_3\text{O}_4\text{-MWCNT})_{20}$  multilayers. (c) The average mass density of the  $\text{NH}_2\text{-MWCNT/OA-Fe}_3\text{O}_4\text{-MWCNT}$  multilayers that was calculated from the linear slope of mass per unit area vs. film thickness curve. (d) Total film thicknesses of the  $(\text{NH}_2\text{-MWCNT/OA-Fe}_3\text{O}_4\text{-MWCNT})_n$  and  $(\text{NH}_3^+\text{-MWCNT/anionic octakis-Fe}_3\text{O}_4\text{-MWCNT})_n$  multilayers measured from the cross-sectional FE-SEM images. In addition, the solution concentrations of the  $\text{OA-Fe}_3\text{O}_4\text{-MWCNT}$ s and anionic octakis- $\text{Fe}_3\text{O}_4\text{-MWCNT}$ s were adjusted to be approximately  $11 \text{ mg mL}^{-1}$ . (e) The film thicknesses of the  $(\text{NH}_2\text{-MWCNT/OA-Fe}_3\text{O}_4\text{-MWCNT})_n$  multilayers as the solution concentration of the  $\text{OA-Fe}_3\text{O}_4\text{-MWCNT}$  hybrids was changed from 11 to 22  $\text{mg mL}^{-1}$ .

within the  $\text{NH}_2\text{-MWCNT/OA-Fe}_3\text{O}_4\text{-MWCNT}$  multilayers, facilitating the infiltration of MWCNTs within the porous multilayers as well as the removal of insulating OA ligands bound to the surface of the  $\text{Fe}_3\text{O}_4$  NPs during LbL deposition. Additionally, porous  $\text{NH}_2\text{-MWCNT/OA-Fe}_3\text{O}_4\text{-MWCNT}$  multilayers were more effective at facilitating ion and electron transfer compared to the insulating  $\text{PEI/OA-Fe}_3\text{O}_4\text{-MWCNT}$  multilayers with the same film thickness.

The porosity of the  $\text{NH}_2\text{-MWCNT/OA-Fe}_3\text{O}_4\text{-MWCNT}$  multilayers was also investigated by  $\text{N}_2$  adsorption-desorption

(Fig. 4b). In this case, the BET specific surface area and the pore volume of  $\text{NH}_2\text{-MWCNT/OA-Fe}_3\text{O}_4\text{-MWCNT}$  multilayers were calculated to be  $67.21 \text{ m}^2 \text{ g}^{-1}$  and  $0.29 \text{ cm}^3 \text{ g}^{-1}$ , respectively. The surface area of pristine MWCNTs has been reported to be approximately  $10\text{--}20 \text{ m}^2 \text{ g}^{-1}$ .<sup>46</sup> Additionally, the multilayer sample had a small diameter of approximately 3 nm and a relatively large diameter ranging from 16 to 44 nm (obtained by Barrett-Joyner-Halenda (BJH) analysis).

Furthermore, given that these  $\text{Fe}_3\text{O}_4$  NPs are high-energy-density materials with pseudocapacitive properties,

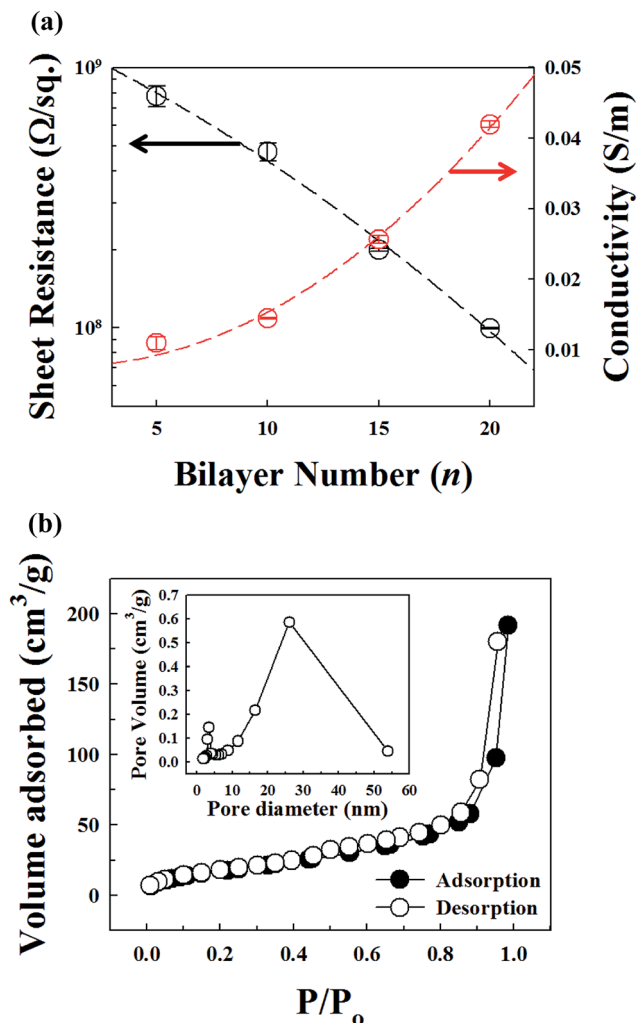


Fig. 4 (a) Sheet resistance and electrical conductivity of the  $(\text{NH}_2\text{-MWCNT/OA-Fe}_3\text{O}_4\text{-MWCNT})_n$  multilayer films as a function of the bilayer number ( $n$ ). These films were prepared using a solution concentration of  $11 \text{ mg mL}^{-1}$  OA- $\text{Fe}_3\text{O}_4\text{-MWCNT}$  in toluene and  $1 \text{ mg mL}^{-1}$   $\text{NH}_2\text{-MWCNT}$  in ethanol. (b)  $\text{N}_2$  adsorption-desorption isotherm and the pore size distribution (inset) of  $\text{NH}_2\text{-MWCNT/OA-Fe}_3\text{O}_4\text{-MWCNT}$  multilayer.

postulating that these nanocomposite multilayers, including densely packed  $\text{Fe}_3\text{O}_4$  NPs, can be used as high-performance supercapacitor electrodes<sup>30,47-53</sup> with excellent volumetric capacitance in a limited electrode volume is counterintuitive. To confirm this possibility, we first investigated the charge storage capacities of  $\text{NH}_2\text{-MWCNT/OA-Fe}_3\text{O}_4\text{-MWCNT}$  multilayers deposited onto ITO electrodes using a three-electrode cell. CV curves of multilayer electrodes were measured at various scan rates ranging from 5 to  $100 \text{ mV s}^{-1}$  in 1 M  $\text{Na}_2\text{SO}_3$  electrolyte instead of a harsh acidic electrolyte. These measurements were also performed in a potential window between  $-0.9 \text{ V}$  and  $+0.1 \text{ V}$  to prevent degradation of the electrode and electrolyte at higher potentials. Fig. 5a displays the CV data for the  $(\text{NH}_2\text{-MWCNT/OA-Fe}_3\text{O}_4\text{-MWCNT})_{n=5-20}$  electrodes at a scan rate of  $5 \text{ mV s}^{-1}$  as a function of the bilayer number ( $n$ ). The geometric current density level of the

asymmetric CV curve with a redox peak increased with increasing bilayer number (or total film thickness) of the multilayer electrode. According to previous reports,<sup>19,54</sup> the redox behavior of  $\text{Fe}_3\text{O}_4$  NPs in  $\text{Na}_2\text{SO}_3$  solution originates from multi-electron redox reactions, corresponding to both the surface redox reactions of sulfur in the form of sulfate and sulfite anions adsorbed onto the surface of  $\text{Fe}_3\text{O}_4$  NPs and the redox reaction between  $\text{Fe}^{\text{II}}$  and  $\text{Fe}^{\text{III}}$ . For a more detailed analysis, the charge storage capacity per unit area (or the total integrated charge density (in  $\text{mC cm}^{-2}$ )) was calculated using the integrated area of the bilayer number-dependent CV curves shown in Fig. 5a. In this case, the charge storage density of the  $\text{NH}_2\text{-MWCNT/OA-Fe}_3\text{O}_4\text{-MWCNT}$  multilayer electrodes increased nearly linearly with respect to the bilayer number of the multilayer electrodes, suggesting that the charge storage capacity of the multilayer electrodes could be further enhanced and precisely controlled by adjusting the bilayer number (Fig. 5b). The CV curves of the  $\text{NH}_2\text{-MWCNT/COOH-MWCNT}$  multilayer electrode without pseudocapacitive  $\text{Fe}_3\text{O}_4$  NPs and the  $\text{NH}_3^+\text{-MWCNT/anionic octakis-Fe}_3\text{O}_4\text{-MWCNT}$  multilayer electrode with a low packing density ( $<30\%$ ) of  $\text{Fe}_3\text{O}_4$  NPs exhibited a relatively symmetrical and rectangular shape without evident redox peaks, similar to the characteristics of double-layer capacitance (Fig. S7<sup>†</sup>). By contrast, the  $\text{NH}_2\text{-MWCNT/OA-Fe}_3\text{O}_4\text{-MWCNT}$  electrode with double-layer capacitance and pseudocapacitance behavior displayed asymmetrical CV curves with evident redox peaks due to the formation of densely packed  $\text{Fe}_3\text{O}_4$  NPs within electrodes. The mass densities of the  $\text{NH}_3^+\text{-MWCNT/anionic octakis-Fe}_3\text{O}_4\text{-MWCNT}$  and  $\text{NH}_2\text{-MWCNT/OA-Fe}_3\text{O}_4\text{-MWCNT}$  multilayer electrodes were approximately  $1.14 \pm 0.03$  and  $1.65 \pm 0.02 \text{ g cm}^{-3}$ , respectively. These results explain why the geometric current level of the 241 nm-thick  $\text{NH}_2\text{-MWCNT/OA-Fe}_3\text{O}_4\text{-MWCNT}$  multilayer electrode is considerably higher than those of the 247 nm-thick  $\text{NH}_2\text{-MWCNT/COOH-MWCNT}$  and 246 nm-thick  $\text{NH}_3^+\text{-MWCNT/anionic octakis-Fe}_3\text{O}_4\text{-MWCNT}$  multilayer electrodes, despite their similar film thicknesses. As a result, the volumetric capacitances of the  $\text{NH}_2\text{-MWCNT/COOH-MWCNT}$ ,  $\text{NH}_3^+\text{-MWCNT/anionic octakis-Fe}_3\text{O}_4\text{-MWCNT}$ , and  $\text{NH}_2\text{-MWCNT/OA-Fe}_3\text{O}_4\text{-MWCNT}$  multilayer electrodes with similar film thicknesses of approximately 241 nm were approximately  $63 \pm 2$ ,  $192 \pm 7$ , and  $289 \pm 10 \text{ F cm}^{-3}$  (specific mass capacitance of approximately  $190 \pm 17 \text{ F g}^{-1}$ ) at  $5 \text{ mV s}^{-1}$ , respectively. In the case of the  $1.37 \mu\text{m}$ -thick  $(\text{NH}_2\text{-MWCNT/OA-Fe}_3\text{O}_4\text{-MWCNT})_{40}$  electrode, its volumetric capacitance decreased to  $221 \text{ F cm}^{-3}$  at  $5 \text{ mV s}^{-1}$  because the thick film electrode blocked the transfer paths of the electrolytic ions. In particular, the volumetric capacitance obtained from the OA- $\text{Fe}_3\text{O}_4\text{-MWCNT}$  hybrid-based electrode was considerably higher than the volumetric capacitance of the conventionally blended nanocomposite<sup>55</sup> or the LbL-assembled  $(\text{MWCNT/MnO}_2 \text{ NP})_n$  electrodes,<sup>28</sup> although the specific capacitance value ( $60\text{--}80 \text{ F g}^{-1}$ ) of the  $\text{Fe}_3\text{O}_4$  NPs<sup>55</sup> has been reported to be significantly lower than the specific capacitance values of other pseudocapacitive NPs such as  $\text{MnO}_2$  (theoretical capacitance value of approximately  $1370 \text{ F g}^{-1}$ ) and  $\text{RuO}_2$  ( $720\text{--}900 \text{ F g}^{-1}$ ). These phenomena were caused mainly by the dense packing of high-

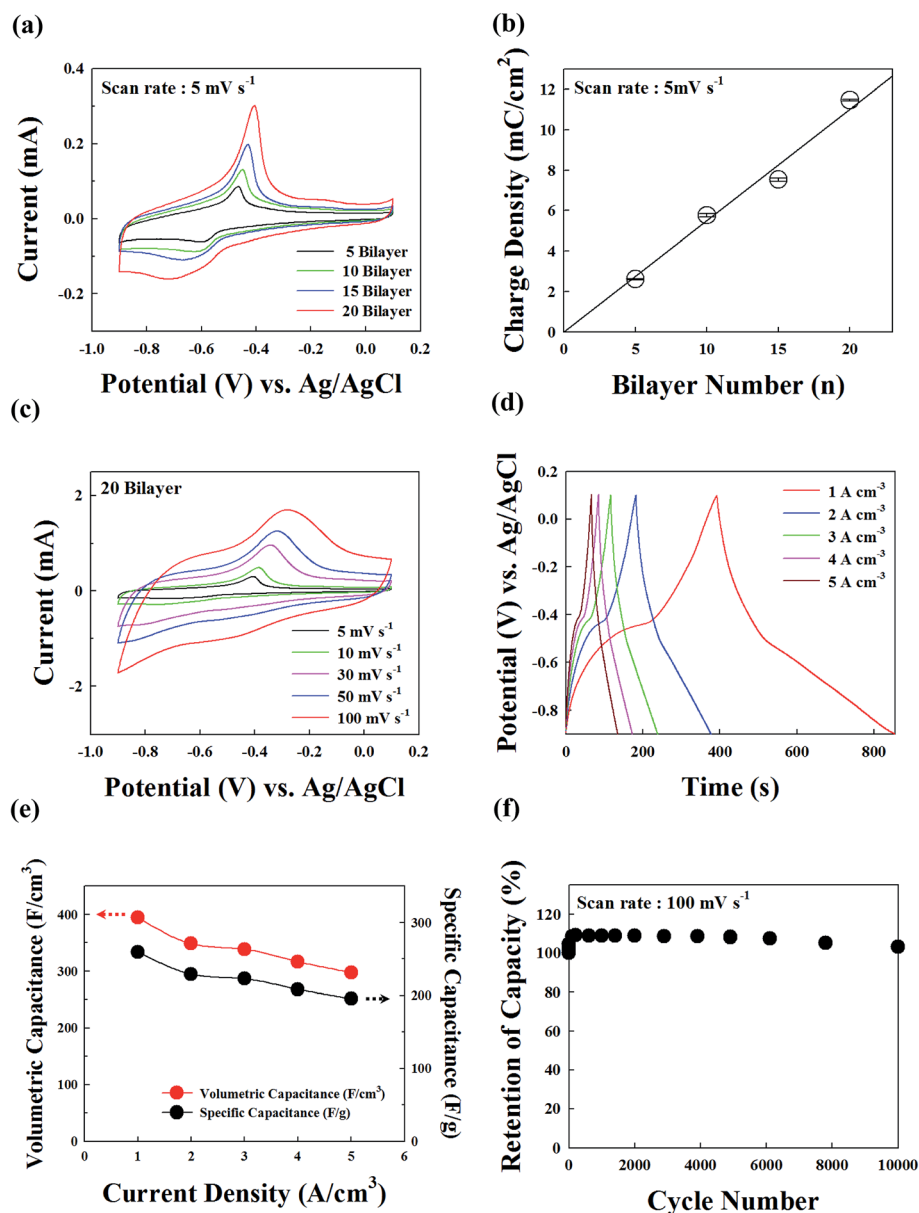


Fig. 5 (a) CV curves and (b) total integrated charge density of the LbL-assembled  $(\text{NH}_2\text{-MWCNT/OA-Fe}_3\text{O}_4\text{-MWCNT})_n$  electrode as a function of bilayer number. In this case, the scan rate was fixed at  $5 \text{ mV s}^{-1}$ . (c) CV curves of the LbL-assembled  $(\text{NH}_2\text{-MWCNT/OA-Fe}_3\text{O}_4\text{-MWCNT})_{20}$  electrode as a function of scan rate (5 to  $100 \text{ mV s}^{-1}$ ). (d) Galvanostatic charge-discharge curves and (e) volumetric and specific capacitance of the LbL-assembled  $(\text{NH}_2\text{-MWCNT/OA-Fe}_3\text{O}_4\text{-MWCNT})_{20}$  electrode as a function of current density (1 to  $5 \text{ A cm}^{-3}$ ). (f) Cycling performance of the  $(\text{NH}_2\text{-MWCNT/OA-Fe}_3\text{O}_4\text{-MWCNT})_{20}$  electrode collected at a scan rate of  $100 \text{ mV s}^{-1}$  for 10 000 cycles.

quality OA-Fe<sub>3</sub>O<sub>4</sub> NPs on the porous MWCNT layers with good access to electrons and ions in the electrolyte.

The NH<sub>2</sub>-MWCNT/OA-Fe<sub>3</sub>O<sub>4</sub>-MWCNT multilayer electrodes also exhibited good pseudocapacitive behavior as the scan rate was increased from 5 to  $100 \text{ mV s}^{-1}$ , implying that the multilayer electrodes possess the properties of relatively fast charge transfer and good rate capability despite the densely packed OA-Fe<sub>3</sub>O<sub>4</sub> NP layers (Fig. 5c and S8†). However, a further increase in the scan rate caused a shift in the peak current toward higher potentials during the charging step because of poor reaction kinetics. Thus, the decrease in volumetric capacitance along with the increase in scan rate implies that the

charges accumulated to the inner active sites of the electrode at low scan rates can be utilized for charge storage. Conversely, at higher scan rates, only the outer active surface of the electrode materials can be used as charge storage sites, which is typical behavior for an electrochemical charge storage system.

These phenomena were also confirmed by the galvanostatic charge-discharge curves of the  $(\text{NH}_2\text{-MWCNT/OA-Fe}_3\text{O}_4\text{-MWCNT})_{20}$  electrode in the volumetric current density range from 1 to  $5 \text{ A cm}^{-3}$ . In this case, the current density of the LbL-assembled multilayer electrode was expressed as the volumetric current density ( $\text{mA cm}^{-3}$ ) to obtain the thickness (*i.e.*, bilayer number)-independent galvanostatic charge-discharge curve. As

shown in Fig. 5d, the slanted parts in the charging potential window in the range from  $-0.6$  to  $-0.4$  V and the discharging potential window in the range from  $-0.5$  to  $-0.7$  V displayed overlapped redox reactions, consistent with the occurrence of redox peaks in the cyclic voltammograms in Fig. 5a. That is, the linear dependence of the potential on time at potentials greater than  $-0.4$  V means that the electrical double-layer capacitance (EDLC) behavior originates from the charge separation at the electrode-electrolyte interface. The time dependence of the potential below  $-0.4$  V was nonlinear because of the pseudo-capacitance behavior of the OA-Fe<sub>3</sub>O<sub>4</sub> within the electrode. In

addition, the (NH<sub>2</sub>-MWCNT/OA-Fe<sub>3</sub>O<sub>4</sub>-MWCNT)<sub>20</sub> multilayer electrode exhibited a longer discharge time compared to that of the conventional NH<sub>2</sub>-MWCNT/COOH-MWCNT capacitor electrodes with similar film thicknesses (Fig. S9†), implying that the OA-Fe<sub>3</sub>O<sub>4</sub>-MWCNT-based electrode has good charge storage performance.<sup>57</sup>

As previously mentioned (see Fig. 5b), the charge storage capacity per unit area of the LbL-assembled electrode increased according to the bilayer number ( $n$ ) of multilayers, which was confirmed by the galvanostatic charge-discharge curves (Fig. S10†). That is, the integrated area of the galvanostatic

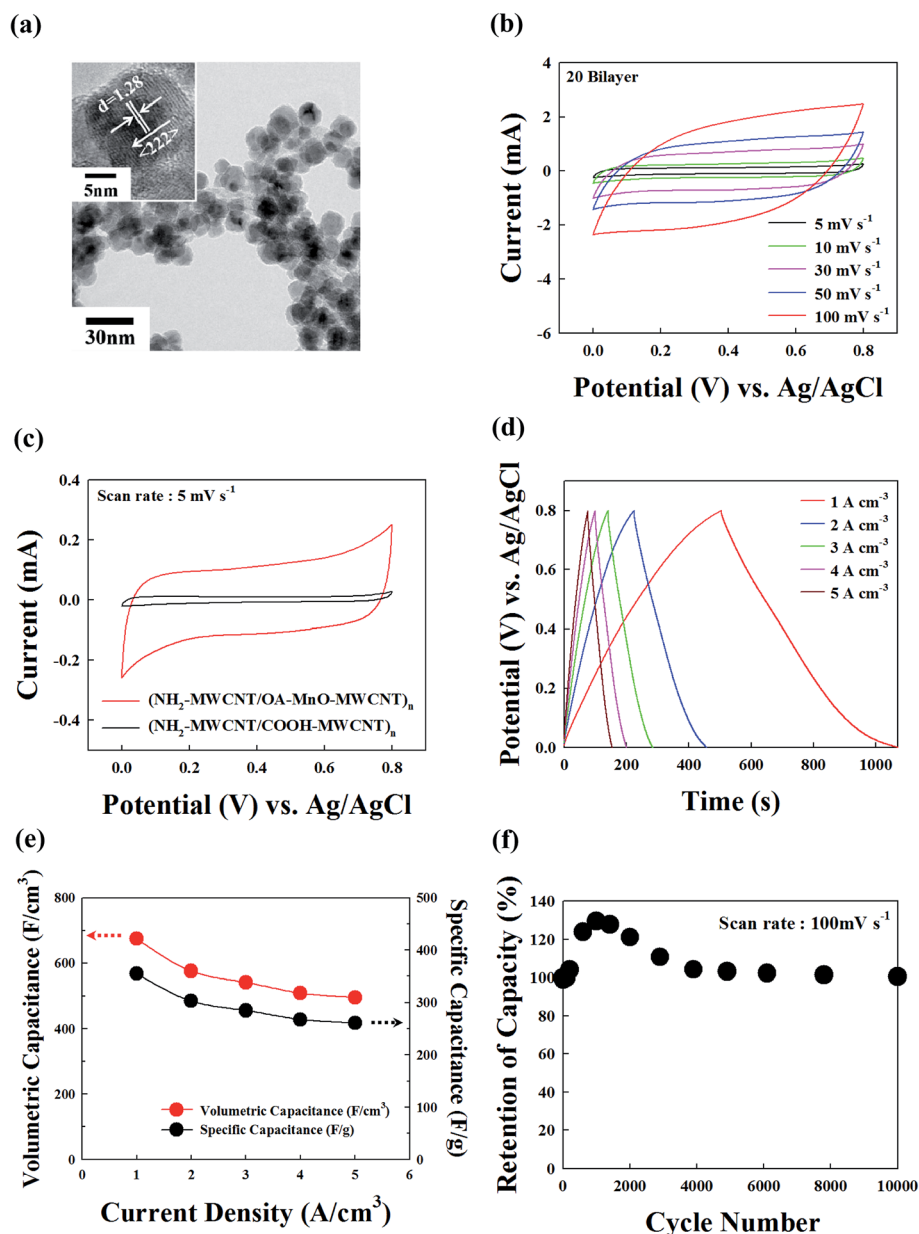


Fig. 6 (a) HR-TEM image of the OA-MnO-MWCNT hybrids. (b) CV curves of the LbL-assembled (NH<sub>2</sub>-MWCNT/OA-MnO-MWCNT)<sub>20</sub> electrode as a function of scan rate. (c) CV curves of the 227 nm-thick NH<sub>2</sub>-MWCNT/COOH-MWCNT, and 219 nm-thick NH<sub>2</sub>-MWCNT/OA-MnO-MWCNT multilayer electrodes measured at a scan rate of 5 mV s<sup>-1</sup>. (d) Galvanostatic charge-discharge curves and (e) volumetric and specific capacitance of the LbL-assembled (NH<sub>2</sub>-MWCNT/OA-MnO-MWCNT)<sub>20</sub> electrode as a function of current density (1 to 5 A cm<sup>-3</sup>). (f) Cycling performance of the (NH<sub>2</sub>-MWCNT/OA-MnO-MWCNT)<sub>20</sub> electrode collected at a scan rate of 100 mV s<sup>-1</sup> for 10 000 cycles.

charge–discharge curve of  $(\text{NH}_2\text{-MWCNT/OA-Fe}_3\text{O}_4\text{-MWCNT})_n$  multilayer electrodes (*i.e.*, the total charge storage capacity of multilayer electrode) increased with increasing the bilayer number ( $n$ ) at a fixed areal current density (*i.e.*,  $0.1 \text{ mA cm}^{-2}$ ). Fig. 5e shows the capacitance of the  $(\text{NH}_2\text{-MWCNT/OA-Fe}_3\text{O}_4\text{-MWCNT})_{20}$  electrode calculated from galvanostatic charge–discharge curves at different current densities (the equation used is shown in the Experimental). The volumetric capacitance was measured to be  $394 \pm 10 \text{ F cm}^{-3}$  (specific capacitance  $\sim 260 \pm 15 \text{ F g}^{-1}$ ) at  $1 \text{ A cm}^{-3}$ , respectively. Furthermore, with an increase in the discharge current density to  $5 \text{ A cm}^{-3}$ , the volumetric capacitance was maintained at  $297 \pm 10 \text{ F cm}^{-3}$  ( $196 \pm 13 \text{ F g}^{-1}$ ). This good rate capability is similar to the results obtained from CV measurements (see Fig. 5c and S8†). These capacitance values were much higher than those of previously reported electrodes based on carbon-based materials and iron oxide NPs (*i.e.*, carbon–iron oxide NP or CNT–iron oxide NP nanocomposite electrodes prepared by simple blending and/or a doctor-blade approach).<sup>58–60</sup>

The long-term cycling performance of the  $(\text{NH}_2\text{-MWCNT/OA-Fe}_3\text{O}_4\text{-MWCNT})_{20}$  electrode was tested over 10 000 cycles at a scan rate of  $100 \text{ mV s}^{-1}$  (Fig. 5f). In this case, the electrode maintained 103% of its initial volumetric capacitance after 10 000 cycles. The conventional electrostatic  $\text{NH}_3^+\text{-MWCNT/}$ anionic octakis- $\text{Fe}_3\text{O}_4\text{-MWCNT}$  multilayer electrode exhibited a 37% loss of initial capacitance after the same number of cycles (Fig. S11†). These results demonstrate that the  $\text{NH}_2\text{-MWCNT/OA-Fe}_3\text{O}_4\text{-MWCNT}$  multilayer electrode formed *via* covalent bonding is more stable than the electrostatically LbL-assembled  $\text{NH}_3^+\text{-MWCNT/}$ anionic octakis- $\text{Fe}_3\text{O}_4\text{-MWCNT}$  multilayer electrode.

On the basis of these results obtained using the  $\text{OA-Fe}_3\text{O}_4\text{-MWCNT}$  hybrids, our approach was further extended to the  $\text{NH}_2\text{-MWCNT/OA-MnO-MWCNT}$  multilayer electrodes for the preparation of a more efficient energy storage device. First,  $15 \pm 1 \text{ nm}$ -sized  $\text{OA-MnO}$  NPs synthesized in toluene were densely coated onto the  $\text{NH}_2\text{-MWCNTs}$  using a ligand exchange reaction (Fig. 6a). These hybrids were then sequentially LbL-assembled with the  $\text{NH}_2\text{-MWCNTs}$  onto ITO electrodes. The electrochemical properties of the resultant  $(\text{NH}_2\text{-MWCNT/OA-MnO-MWCNT})_{20}$  electrodes were investigated in the potential range between 0 V and +0.8 V in 1 M  $\text{Na}_2\text{SO}_4$  solution. As shown in Fig. 6b, these electrodes exhibited good rate capability similar to that of the  $(\text{NH}_2\text{-MWCNT/OA-Fe}_3\text{O}_4\text{-MWCNT})_{20}$  electrodes at scan rates in the range from 5 to  $100 \text{ mV s}^{-1}$ . Fig. 6c shows that  $\text{NH}_2\text{-MWCNT/OA-MnO-MWCNT}$  multilayer electrodes exhibit greater charge storage than the  $\text{NH}_2\text{-MWCNT/COOH-MWCNT}$  multilayer electrode without pseudocapacitive  $\text{MnO}$  NPs. In particular, the volumetric capacitance based on discharge curves of the  $(\text{NH}_2\text{-MWCNT/OA-MnO-MWCNT})_{20}$  electrode was calculated to be approximately  $674 \pm 13 \text{ F cm}^{-3}$  ( $354 \pm 9 \text{ F g}^{-1}$ ) at  $1 \text{ A cm}^{-3}$ ; this capacitance is greater than the values for the  $\text{NH}_2\text{-MWCNT/OA-Fe}_3\text{O}_4\text{-MWCNT}$  multilayer electrodes at the same current density and greater than those previously reported for electrodes based on carbon-based materials and manganese oxide NPs (Fig. 6d and e).<sup>21,23,28,30,61,62</sup> Additionally, the  $(\text{NH}_2\text{-MWCNT/OA-MnO-}$

$\text{MWCNT})_{20}$  electrode also displayed notable electrochemical stability during repeated cycling operations. An increase of approximately 30% in the initial capacitance after 1100 cycles was caused by the enhanced effective interfacial area between the electrolyte and electrode materials as well as by the full activation of the electrode with increasing reaction time.<sup>56,63–66</sup> These phenomena were also observed in the  $(\text{NH}_2\text{-MWCNT/OA-Fe}_3\text{O}_4\text{-MWCNT})_{20}$  electrode (see Fig. 6f). As a result, the initial capacitance of the  $(\text{NH}_2\text{-MWCNT/OA-MnO-MWCNT})_{20}$  electrode was maintained without additional loss until 10 000 cycles, implying that the covalently bonded LbL electrodes formed after the ligand exchange reaction are highly stable electrochemically.

## Conclusions

We demonstrated that the LbL-assembled multilayers using high-energy MWCNTs could be used effectively as a promising electrode material for high-performance energy storage devices without the aid of an additional polymer binder. The volumetric capacitances of the  $(\text{NH}_2\text{-MWCNT/OA-Fe}_3\text{O}_4\text{-MWCNT})_{20}$  and  $(\text{NH}_2\text{-MWCNT/OA-MnO-MWCNT})_{20}$  electrodes were  $394 \pm 10$  and  $674 \pm 13 \text{ F cm}^{-3}$  at  $1 \text{ A cm}^{-3}$ , respectively. The  $\text{NH}_2\text{-MWCNT/OA-PC-MWCNT}$  multilayers maintained their initial capacitance even after 10 000 cycles. This notable operational stability was caused by chemically stable covalent bonding between  $\text{OA-PC}$  NP and  $\text{NH}_2\text{-MWCNTs}$  and between  $\text{OA-PC-MWCNTs}$  and  $\text{NH}_2\text{-MWCNTs}$ . Furthermore, given that MWCNT hybrids with a variety of high-energy PC NPs can easily be prepared in organic media, our approach provides a basis for exploiting and designing high-performance electrochemical electrodes.

## Acknowledgements

This work was supported by the National Research Foundation (NRF) grant funded by the Ministry of Science, ICT & Future Planning (MSIP) (2015R1A2A1A01004354).

## Notes and references

- 1 J. R. Miller and P. Simon, *Science*, 2008, **321**, 651–652.
- 2 A. S. Arico, P. Bruce, B. Scrosati, J.-M. Tarascon and W. V. Schalkwijk, *Nat. Mater.*, 2005, **4**, 366–377.
- 3 S. Park, J. M. Vohs and R. J. Gorte, *Nature*, 2000, **404**, 265–267.
- 4 M. F. El-Kady, V. Strong, S. Dubin and R. B. Kaner, *Science*, 2012, **335**, 1326–1330.
- 5 J. Shen, A. Liu, Y. Tu, G. Foo, C. Yeo, M. B. C. Park, R. Jiang and Y. Chen, *Energy Environ. Sci.*, 2011, **4**, 4220–4229.
- 6 P. Leung, X. Li, C. Ponce de Leon, L. Berlouis, C. T. J. Low and F. C. Walsh, *RSC Adv.*, 2012, **2**, 10125–10156.
- 7 A. Marschilok, C.-Y. Lee, A. Subramanian, K. J. Takeuchi and E. S. Takeuchi, *Energy Environ. Sci.*, 2011, **4**, 2943–2951.
- 8 H. Wang, Y. Liang, M. Gong, Y. Li, W. Chang, T. Mefford, J. Zhou, J. Wang, T. Regier, F. Wei and H. Dai, *Nat. Commun.*, 2012, **3**, 917.

- 9 Z. Zhu, Y. Hu, H. Jiang and C. Li, *J. Power Sources*, 2014, **246**, 402–408.
- 10 Z. Su, C. Yang, B. Xie, Z. Lin, Z. Zhang, J. Liu, B. Li, F. Kang and C. P. Wong, *Energy Environ. Sci.*, 2014, **7**, 2652–2659.
- 11 J.-J. Li, M.-C. Liu, L.-B. Kong, D. Wang, Y.-M. Hu, W. Han and L. Kang, *RSC Adv.*, 2015, **5**, 41721–41728.
- 12 J. Cherusseri and K. K. Kar, *RSC Adv.*, 2015, **5**, 34335–34341.
- 13 R. Li, X. Ren, F. Zhang, C. Du and J. Liu, *Chem. Commun.*, 2012, **48**, 5010–5012.
- 14 P. Simon and Y. Gogotsi, *Nat. Mater.*, 2008, **7**, 845–854.
- 15 Y. Jiang, P. Wang, X. Zang, Y. Yang, A. Kozinda and L. Lin, *Nano Lett.*, 2013, **13**, 3524–3530.
- 16 H. Jiang, Y. Dai, Y. Hu, W. Chen and C. Li, *ACS Sustainable Chem. Eng.*, 2014, **2**, 70–74.
- 17 H. Jiang, J. Ma and C. Li, *Adv. Mater.*, 2012, **24**, 4197–4202.
- 18 S. Chaudhari, D. Bhattacharjya and J.-S. Yu, *RSC Adv.*, 2013, **3**, 25120–25128.
- 19 J. Mu, B. Chen, Z. Guo, M. Zhang, Z. Zhang, P. Zhang, C. Shao and Y. Liu, *Nanoscale*, 2011, **3**, 5034–5040.
- 20 A. B. Deshmukh and M. V. Shelke, *RSC Adv.*, 2013, **3**, 21390–21393.
- 21 Z. Lei, F. Shi and L. Lu, *ACS Appl. Mater. Interfaces*, 2012, **4**, 1058–1064.
- 22 Z. Fan, J. Yan, T. Wei, L. Zhi, G. Ning, T. Li and F. Wei, *Adv. Funct. Mater.*, 2011, **21**, 2366–2375.
- 23 Y. Cheng, S. Lu, H. Zhang, C. V. Varanasi and J. Liu, *Nano Lett.*, 2012, **12**, 4206–4211.
- 24 X. Lang, A. Hirata, T. Fujita and M. Chen, *Nat. Nanotechnol.*, 2011, **6**, 232–236.
- 25 Y. Gogotsi and P. Simon, *Science*, 2011, **334**, 917–918.
- 26 S. Murali, N. Quarles, L. L. Zhang, J. R. Potts, Z. Tan, Y. Lu, Y. Zhu and R. S. Ruoff, *Nano Energy*, 2013, **2**, 764–768.
- 27 S. W. Lee, B.-S. Kim, S. Chen, Y. Shao-Horn and P. T. Hammond, *J. Am. Chem. Soc.*, 2009, **131**, 671–679.
- 28 S. W. Lee, J. Kim, S. Chen, P. T. Hammond and Y. Shao-Horn, *ACS Nano*, 2010, **4**, 3889–3896.
- 29 T. Lee, S. H. Min, M. Gu, Y. K. Jung, W. Lee, J. U. Lee, D. G. Seong and B.-S. Kim, *Chem. Mater.*, 2015, **27**, 3785–3796.
- 30 M. N. Hyder, B. M. Gallant, N. J. Shah, Y. Shao-Horn and P. T. Hammond, *Nano Lett.*, 2013, **13**, 4610–4619.
- 31 Y. Ko, H. Baek, Y. Kim, M. Yoon and J. Cho, *ACS Nano*, 2013, **7**, 143–153.
- 32 Y. Ko, D. Shin, B. Koo, S. W. Lee, W.-S. Yoon and J. Cho, *Nano Energy*, 2014, **12**, 612–625.
- 33 S. E. Baker, W. Cai, T. L. Lasseter, K. P. Weidkamp and R. J. Hamers, *Nano Lett.*, 2002, **2**, 1413–1417.
- 34 T.-K. Hong, D. W. Lee, H. J. Choi, H. S. Shin and B.-S. Kim, *ACS Nano*, 2010, **4**, 3861–3868.
- 35 T. Ramanathan, F. T. Fisher, R. S. Ruoff and L. C. Brinson, *Chem. Mater.*, 2005, **17**, 1290–1295.
- 36 S. Sun, H. Zeng, D. B. Robinson, S. Raoux, P. M. Rice, S. X. Wang and G. Li, *J. Am. Chem. Soc.*, 2004, **126**, 273–279.
- 37 F. Su, C. Lu and H.-S. Chen, *Langmuir*, 2011, **27**, 8090–8098.
- 38 H. C. Choi, S. Y. Bae and J. Park, *Appl. Phys. Lett.*, 2004, **85**, 5742–5744.
- 39 A. Misra, P. K. Tyagi, M. K. Singh and D. S. Misra, *Diamond Relat. Mater.*, 2006, **15**, 385–388.
- 40 A. K. Mishra and S. Ramaprabhu, *Energy Environ. Sci.*, 2011, **4**, 889–895.
- 41 P. Nayak, B. Anbarasan and S. Ramaprabhu, *J. Phys. Chem. C*, 2013, **117**, 13202–13209.
- 42 K. Shimizu, J. S. Wang and C. M. Wai, *J. Phys. Chem. A*, 2010, **114**, 3956–3961.
- 43 L. Han, W. Wu, F. L. Kirk, J. Luo, M. M. Maye, N. N. Kariuki, Y. Lin, C. Wang and C.-J. Zhong, *Langmuir*, 2004, **20**, 6019–6025.
- 44 M.-S. Cao, J. Yang, W.-L. Song, D.-Q. Zhang, B. Wen, H.-B. Jin, Z.-L. Hou and J. Yuan, *ACS Appl. Mater. Interfaces*, 2012, **4**, 6949–6956.
- 45 D. Buttry, *Advances in Electroanalytical Chemistry: Applications of the QCM to Electrochemistry*, Marcel Dekker, New York, 1991.
- 46 P. M. Ajayan, *Chem. Rev.*, 1999, **99**, 1787–1799.
- 47 E. Frackowiak and F. Beguin, *Carbon*, 2001, **39**, 937–950.
- 48 J. Lee, S. Yoon, T. Hyeon, S. M. Oh and K. B. Kim, *Chem. Commun.*, 1999, 2177–2178.
- 49 H. Jiang, P. S. Lee and C. Li, *Energy Environ. Sci.*, 2013, **6**, 41–53.
- 50 C. Guan, J. Liu, Y. Wang, L. Mao, Z. Fan, Z. Shen, H. Zhang and J. Wang, *ACS Nano*, 2015, **9**, 5198–5207.
- 51 H. Wang and H. Dai, *Chem. Soc. Rev.*, 2013, **42**, 3088–3113.
- 52 M. Zhi, C. Xiang, J. Li, M. Li and N. Wu, *Nanoscale*, 2013, **5**, 72–88.
- 53 A. L. M. Reddy, M. M. Shaijumon, S. R. Gowda and P. M. Ajayan, *J. Phys. Chem. C*, 2010, **114**, 658–663.
- 54 N.-L. Wu, S.-Y. Wang, C.-Y. Han, D.-S. Wu and L.-R. Shiu, *J. Power Sources*, 2003, **113**, 173–178.
- 55 M. B. Sassin, A. N. Mansour, K. A. Pettigrew, D. R. Rolison and J. W. Long, *ACS Nano*, 2010, **4**, 4505–4514.
- 56 W. Shi, J. Zhu, D. H. Sim, Y. Y. Tay, Z. Lu, X. Zhang, Y. Sharma, M. Srinivasan, H. Zhang, H. H. Hng and Q. Yan, *J. Mater. Chem.*, 2011, **21**, 3422–3427.
- 57 S.-I. Kim, J.-S. Lee, H.-J. Ahn, H.-K. Song and J.-H. Jang, *ACS Appl. Mater. Interfaces*, 2013, **5**, 1596–1603.
- 58 D. Guan, Z. Gao, W. Yang, J. Wang, Y. Yuang, B. Wang, M. Zhang and L. Liu, *Mater. Sci. Eng., B*, 2013, **178**, 736–743.
- 59 C. Fu, A. Mahadevegowda and P. S. Grant, *J. Mater. Chem. A*, 2015, **3**, 14245–14253.
- 60 D. Liu, X. Wang, X. Wang, W. Tian, J. Liu, C. Zhi, D. He, Y. Bando and D. Golberg, *J. Mater. Chem. A*, 2013, **1**, 1952–1955.
- 61 A. E. Fischer, M. P. Saunders, K. A. Pettigrew, D. R. Rolison and J. W. Long, *J. Electrochem. Soc.*, 2008, **155**, A246–A252.
- 62 J. W. Lee, A. S. Hall, J.-D. Kim and T. E. Mallouk, *Chem. Mater.*, 2012, **24**, 1158–1164.
- 63 J. Pu, L. Shen, S. Zhu, J. Wang, W. Zhang and Z. Wang, *J. Solid State Electrochem.*, 2014, **18**, 1067–1076.
- 64 H. Jiang, T. Zhao, C. Yan, J. Ma and C. Li, *Nanoscale*, 2010, **2**, 2195–2198.
- 65 H. Xia, D. Zhu, Z. Luo, Y. Yu, X. Shi, G. Yuan and J. Xie, *Sci. Rep.*, 2013, **3**, 2978.
- 66 T. Wang, Z. Peng, Y. Wang, J. Tang and G. Zheng, *Sci. Rep.*, 2013, **3**, 2693.